PCCP

Cite this: *Phys. Chem. Chem. Phys.*, 2012, **14**, 767–778

www.rsc.org/pccp

PAPER

Nanoscale connectivity in a TiO_2/CdSe quantum dots/functionalized graphene oxide nanosheets/Au nanoparticles composite for enhanced photoelectrochemical solar cell performance†

Remya Narayanan,[a] Melepurath Deepa*[a] and Avanish Kumar Srivastava[b]

Received 8th August 2011, Accepted 31st October 2011
DOI: 10.1039/c1cp22548k

Electron transfer dynamics in a photoactive coating made of CdSe quantum dots (QDs) and Au nanoparticles (NPs) tethered to a framework of ionic liquid functionalized graphene oxide (FGO) nanosheets and mesoporous titania (TiO_2) was studied. High resolution transmission electron microscopy analyses on TiO_2/CdSe/FGO/Au not only revealed the linker mediated binding of CdSe QDs with TiO_2 but also, surprisingly, revealed a nanoscale connectivity between CdSe QDs, Au NPs and TiO_2 with FGO nanosheets, achieved by a simple solution processing method. Time resolved fluorescence decay experiments coupled with the systematic quenching of CdSe emission by Au NPs or FGO nanosheets or by a combination of the latter two provide concrete evidences favoring the most likely pathway of ultrafast decay of excited CdSe in the composite to be a relay mechanism. A balance between energetics and kinetics of the system is realized by alignment of conduction band edges, whereby, CdSe QDs inject photogenerated electrons into the conduction band of TiO_2, from where, electrons are promptly transferred to FGO nanosheets and then through Au NPs to the current collector. Conductive-atomic force microscopy also provided a direct correlation between the local nanostructure and the enhanced ability of composite to conduct electrons. Point contact *I–V* measurements and average photoconductivity results demonstrated the current distribution as well as the population of conducting domains to be uniform across the TiO_2/CdSe/FGO/Au composite, thus validating the higher photocurrent generation. A six-fold enhancement in photocurrent and a 100 mV increment in photovoltage combined with an incident photon to current conversion efficiency of 27%, achieved in the composite, compared to the inferior performance of the TiO_2/CdSe/Au composite imply that FGO nanosheets and Au NPs work in tandem to promote charge separation and furnish less impeded pathways for electron transfer and transport. Such a hierarchical rapid electron transfer model can be adapted to other nanostructures as well, as they can favorably impact photoelectrochemical performance.

1. Introduction

Quantum dot sensitized solar cells (QDSSCs) have attracted widespread attention as they offer an inexpensive means to fabricate photovoltaic devices of reasonably high efficiencies.[1,2] Another specific advantage is that the absorption spectrum of the semiconductor quantum dot can be tailored by simply altering the size of the dot. Hitherto, a plethora of architectures for QDSSCs employing inorganic QDs such as CdS,[3] CdSe,[4] PbS,[5] InP,[6] ZnSe,[7] PbSe,[8] and InAs[9] adsorbed onto wide gap semiconducting oxides like ZnO, TiO_2 and SnO_2 have been proposed and their applicability to visible light harvesting has been investigated. Although the efficiency of QDSSCs continues to be lower than that of traditional dye sensitized solar cells (DSSCs),[10] the ease of processing QDs by wet colloid chemistry, adjustable band gap and their capability to generate more electron–hole pairs from a single photon impingement render them as promising candidates for practical use. Quantum confinement, mini band and Auger recombination effects are cumulatively known to boost exciton concentration, quantum yield, hot electron life time and as a consequence, the overall efficiency of QDSSCs.[11–14]

Among various QDSSCs developed and studied to date, an overall power conversion efficiency of 1%, attained under one sun illumination for an electrode constituted by CdSe QDs

[a] *Department of Chemistry, Indian Institute of Technology Hyderabad, Yeddumailaram-502205, Andhra Pradesh, India. E-mail: mdeepa@iith.ac.in*
[b] *National Physical Laboratory, Dr. K.S. Krishnan road, New Delhi-11001, India*

† Electronic supplementary information (ESI) available: EDS plot and Raman spectrum of FGO nanosheets and a discussion on formation of FGO nanosheets, HRTEM images of TiO_2/CdSe, Tauc plots, absorption quenching of Au NPs by CdSe QDs and emission decay of TiO_2/CdSe films. See DOI: 10.1039/c1cp22548k

flanked to TiO_2 *via* an organic linker, was notable.[15] More recently, a hybrid sensitizer composed of CdSe QDs and a Ru-based molecular dye adsorbed onto mesoscopic TiO_2 has been shown to possess a maximum efficiency of 4.76%.[16] In another report, the focus was on developing a new design by forming an intricate assembly of an antenna layer of QDs coupled with a squaraine dye and TiO_2,[17] which yielded a maximum incident photon to current conversion efficiency (IPCE) of about 10% whilst simultaneously utilizing the full visible spectrum. In yet another study, an IPCE of ~27% (λ = 400 nm) was achieved for a cell based on a composite of graphene–ZnO nanorods CdSe QDs.[18] In a recent development, an IPCE of 70% was obtained for a hierarchical system comprising porphyrin, ZnO nanoparticles and reduced graphene oxide (RGO), by the virtue of fast and efficient electron transfer vis-à-vis a cascade protocol.[19] An efficiency of 1.7% (under 1 sun) has been reported for an electrophoretically deposited CdSe QDs–mesoporous TiO_2 based cell.[20] Most striking was an IPCE of ~60% obtained by reducing the size of the QD surface capping ligand for a system encompassing CdSe QDs bound to nanocrystalline TiO_2.[21]

It has been established that the efficiency of QDSSCs is limited by several factors, which include a non-uniform surface coverage and weak anchoring of QDs to the transition metal oxide, broad size distribution of QDs, sluggish photoexciton generation, and little control over recombination; all maximizing photocurrent losses. One approach to alleviate poor electron transport and transfer from the photoanode to the external circuit involves the tethering of carbon nanotubes (CNTs) or graphene based nanostructures[22,23] to the photosensitizer–semiconducting oxide couple. The electron accepting ability of the carbon nano-object facilitates both electron transport and transfer, thus minimizing losses and improving photocurrent generation. In the past, reports on various assemblies such as stacked cup CNTs–SnO_2,[24] single walled CNTs–TiO_2,[25] graphene oxide–CdS,[26] graphene–Ag nanoparticles (NPs)–TiO_2[27] and porphyrin–graphene[19] have successfully demonstrated the role of the carbon nanostructure in enhancing photocurrent. Another strategy commonly adopted for increasing charge separation involves the adsorption of noble metal nanoparticles like Au or Ag on a scaffold like TiO_2; a space charge layer is formed at the semiconductor–metal interface for Fermi level equilibration and as a consequence, the excited electron is rapidly transferred to the metal nanoparticle which behaves as an electron sink and stores electrons.[28] In a previous study on CdSe QDs sensitized onto Au/TiO_2 hybrid films,[29] authors used a non-covalent approach to adsorb QDs, which can lead to their uncontrolled leaching during photoelectrochemical measurements, and the electron transfer kinetics was not evaluated.

In view of the aforesaid extensive efforts devoted to maximizing the efficiency of photocurrent generation by use of diverse methodologies, in this study, we report the fabrication of a novel nanocomposite constituted by CdSe QDs/Au NPs tethered to a coating of ionic liquid functionalized graphene oxide (FGO) nanosheets and mesoporous titania (TiO_2). Heretofore unreported, the nanostructured assembly was coated on a transparent conducting substrate, by first forming a coating comprising of TiO_2 nanoparticles adsorbed onto FGO nanosheets and then employing the conventional protocol of anchoring CdSe QDs onto this three dimensional framework of TiO_2/FGO with an organic linker as the bridge. The sulfurs on the linker also serve as binding sites for Au nanoparticles,[30] which were introduced along with the QDs. In particular, much emphasis has been laid on characterizing the microstructure of the composite deposit, as morphology is known to have a profound effect on the performance of the photoanode. The excited state interactions involving charge propagation between all the four components of the composite have been followed by fluorescence quenching and by studying the ultrafast kinetics of photogenerated charge carrier decay. The role of each nanomoiety in the composite, *i.e.* CdSe as the exciton generator, Au nanoparticles as an electron sink, functionalized graphene oxide for promoting electron transport and TiO_2 as the robust support, all cumulatively leading to enhanced photocurrent and photovoltage has been rationally analyzed by comparing the performance and properties of individual/twin/ternary components with that of the composite. This work therefore attempts to furnish an understanding of pertinent factors, which control charge transfer and kinetics in QDSSCs, and thus will be relevant for creating new photoanode architectures for high efficiency cells.

2. Results and discussion

2.1 High resolution transmission electron microscopy (HRTEM) studies

Fig. 1a is a low magnification image of exfoliated graphene oxide functionalized by imidazolium triflate (FGO). Since the exfoliation of graphite rods was performed under ambient conditions, the introduction of oxygen containing species on the nanosheets cannot be ruled out.[31] The entrapping of the ionic liquid cation and anion in the FGO nanosheets was confirmed by energy dispersive X-ray analysis (EDS), which showed clear signals due to N, S and F arising from the imidazolium and triflate ions and also by Raman spectroscopy (Fig. S1, ESI†). The nanosheets are entangled with one another and wrinkles and foldings are observed on the surface as well as edges. The overlapping of nanosheets produces the crisscross lattice fringes, as can be seen in the high magnification image shown in Fig. 1b. The defects in the structure, introduced by the action of the ionic liquid and oxygen containing functionalities, show up in the image in the form of ripples. In some regions (inset of Fig. 1c), the hexagonal lattice on the graphene nanosheet could be identified; a blown up view of the quasi-hexagonal arrangement of carbon atoms is presented in Fig. 1c. The slight difference in contrast for the atom in the center is suggestive of a foreign atom like oxygen. The image of the TiO_2/CdSe/FGO/Au composite reveals layers of crinkled FGO nanosheets (Fig. 1d) and from the Fast Fourier Transformation performed on a small region of the film, the electron diffraction pattern, thus obtained, showed a hexagonal array of bright spots, confirming that the high crystalline quality of the FGO nanosheets is preserved in the composite. The CdSe QD size was estimated to be ~3.9 nm, from TEM images, shown in Fig. S2 (ESI†). A series of high magnification images were recorded for the composite, in order

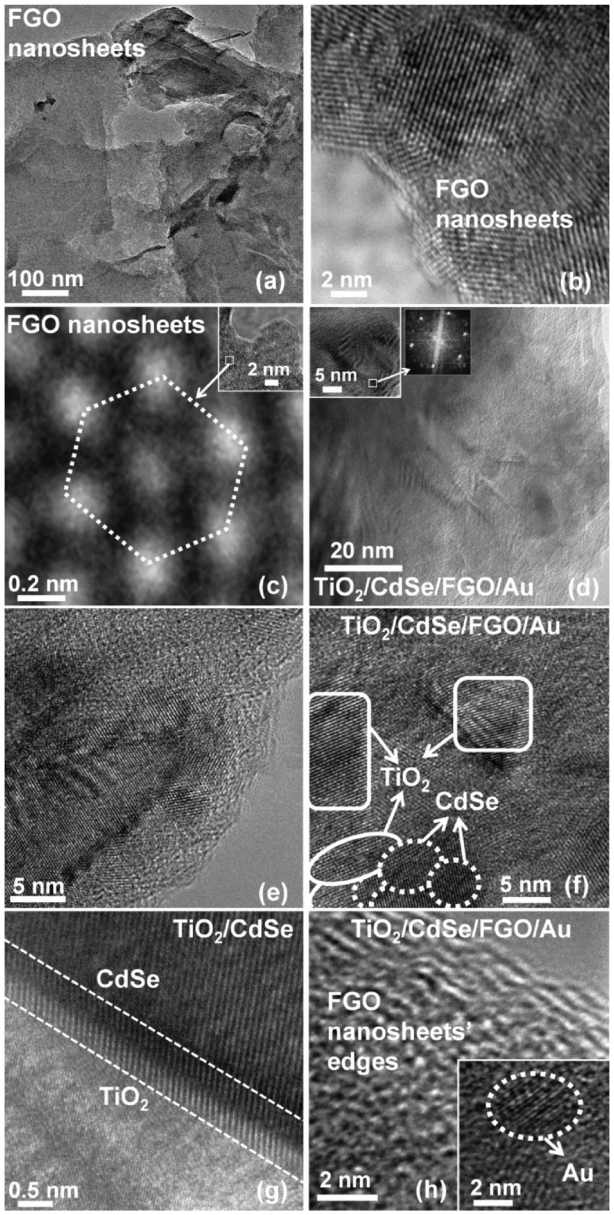

Fig. 1 (a) Low magnification image of crinkled FGO nanosheets, HRTEM images of (b) overlapping FGO nanosheets, (c) atomic scale image of the hexagonal lattice of carbon atoms obtained from a region shown in the inset, (d) HRTEM image of TiO_2/CdSe/FGO/Au composite, the inset is the spotty electron diffraction pattern generated by Fast Fourier Transformation performed on a small region of the composite (shown in the left hand side inset), (e) a blown up view of the TiO_2/CdSe/FGO/Au composite, with overlapping lattice fringes; contributions from all the components, (f) lattice spacings from TiO_2 and CdSe QDs flanked to FGO nanosheets, (g) magnified view of a TiO_2/CdSe QD interface and (h) Au NPs anchored to FGO nanosheets (inset showcases one Au crystallite).

to confirm the distribution of TiO_2, CdSe QDs, FGO nanosheets and Au NPs in the composite. A typical image is shown in Fig. 1e; the fringes are fuzzy in some portions probably due to overlapping of the contributions from different moieties, and it appears that CdSe QDs, TiO_2 and Au NPs are flanked to FGO nanosheets. In some regions, distinctive lattice spacings from TiO_2 with a periodicity of 0.127 nm (JCPDS: 89-4921) and dark fringes with a 0.149 nm separation that originate from CdSe were clearly seen to be embedded in the FGO nanosheets (Fig. 1f). Further evidence affirming the attachment of CdSe QDs with TiO_2 was obtained in the form of a clear interface, shown in Fig. 1g, wherein the bright and dark fringes originate from TiO_2 and CdSe QDs respectively. The change in contrast of the lattice fringes at the boundary of the two moieties is due to the molecular level linking of the two, and also could be due to the presence of the bulky TOPO ligands surrounding the CdSe QDs. The edges of the FGO nanosheets are visible in Fig. 1h, and the inset shows an Au crystallite implanted in the FGO nanosheets. The average Au NP size was $\sim$3 nm, and the fringe separation of 0.123 nm agrees well with the face centered cubic lattice of Au (JCPDS: 65-2870). It is apparent that CdSe QDs, FGO nanosheets, Au NPs and TiO_2 are homogeneously dispersed in the composite, as only a connection between these nano-moieties at the molecular level can account for the HRTEM observations.

2.2 Absorption and fluorescence quenching studies

The digital photographs of the precursor sols of CdSe QDs, Au NPs, FGO nanosheets and their mixtures are shown in Fig. 2A. The suspension of FGO (Fig. 1A(c)) shows the nanosheets to be dispersed homogeneously in toluene, and there is no phase separation or accumulation of particles at the bottom. The colloid comprising FGO nanosheets, Au NPs, and CdSe QDs (Fig. 1A(g)), representative of the composite

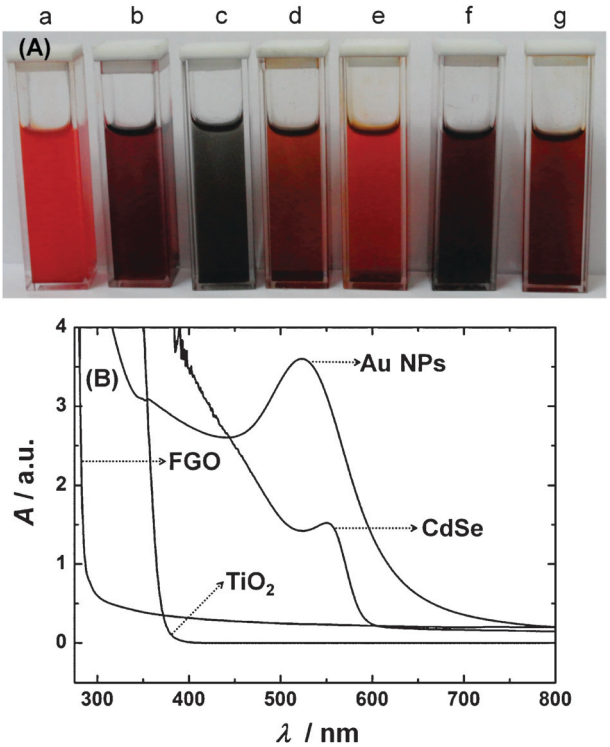

Fig. 2 (A) Digital photographs of solutions of (a) CdSe QDs, (b) Au NPs, (c) FGO nanosheets, (d) CdSe QDs + Au NPs, (e) CdSe + FGO nanosheets, (f) FGO nanosheets + Au NPs and (g) CdSe + Au NPs + FGO nanosheets, (from left to right) and (B) absorbance *versus* wavelength plots of colloids of neat Au NPs, neat FGO nanosheets and neat CdSe QDs. Absorption spectrum of the TiO_2 film is generated from the response in the diffuse reflectance mode.

employed herein for superior photoelectrochemical performance, also displays no signs of aggregation, indicating its suitability for achieving a particulate free adsorption on TiO_2. Fig. 2B shows the absorption spectra of Au NPs, CdSe QDs, TiO_2 nanopowder and FGO nanosheets. Au NPs show an intense absorption peak at 525 nm attributable to the surface plasmon resonance and CdSe QDs show a weak band gap excitation peak at 551 nm, corresponding to a HOMO–LUMO gap of 2.02 eV (Fig. S3, ESI†). Both FGO and TiO_2 show a flat absorption in the visible region. Band gaps were determined from Tauc plots, which are provided in Fig. S3 (ESI†). To comprehend the charge transfer dynamics in the composite (TiO_2/CdSe/FGO/Au), we examined the interplay of the individual components, in terms of fluorescence quenching effects. The band edge emission peak of CdSe QDs is found to lie in the range of 500–700 nm, depending upon the size of the dot.[32–34] The average size of CdSe QD nanocrystals has been found to be ~3.9 nm (Fig. S1, ESI†) and the neat CdSe QD dispersion showed an intense emission peak at 570 nm (Fig. 3a). Previously, TOPO capped CdSe QDs of 4.5 nm dimensions also showed an emission peak at 590 nm.[35] Evidence for charge transfer from CdSe QDs to Au NPs was obtained by following the fluorescence quenching of the CdSe QDs with increasing Au concentration. CdSe QDs strength was fixed at 3 mM, to which a 4 mM Au NP dispersion was added in small aliquots, whilst maintaining the total volume at a fixed value. The progressive decay of the emission of CdSe QDs, with increasing content of Au NPs, is an indicator of the transfer of photogenerated electrons from the conduction band of the donor (CdSe QDs) to the empty electronic states of the Au NPs. We found at a volume ratio of 1 : 2 (CdSe QDs : Au NPs), the fluorescence of QDs almost reduced to negligible values, as can be gauged from the inset of Fig. 3a, suggesting an efficient charge transfer. The corresponding drop in the plasmonic absorption peak of Au NPs seen at 525 nm (Fig. S4, ESI†), as a function of CdSe QD loading, concurs with the aforesaid charge transfer phenomenon.

To investigate further, the effect of FGO nanosheets on the emission of CdSe QDs was studied (Fig. 3b). It has been demonstrated in the past that graphene exfoliated with a di-alkyl imidazolium tetrafluoroborate ionic liquid shows a fairly intense blue emission, typically in the range of 350–450 nm.[36] This emission, in all likelihood, arises from the emitting centers on RGO surfaces, that primarily include the oxygen containing species, like epoxy, carbonyl and hydroxyl groups, for even though, here we employed an IL to exfoliate graphite, the possibility of having oxygen moieties flanked to the graphene nanosheets in the final product (FGO) cannot be ruled out. FGO prepared herein also encompasses the ionic liquid, namely, the 1-butyl-3-methyl-imidazolium ion, which interacts with the GO nanosheets vis-à-vis (a) π–π and (b) electrostatic interactions, and therefore, these defect sites can act as emissive sites and give rise to the emission at ~500 nm, as observed for a pure suspension of FGO (Fig. 3b). The luminescence peak of neat

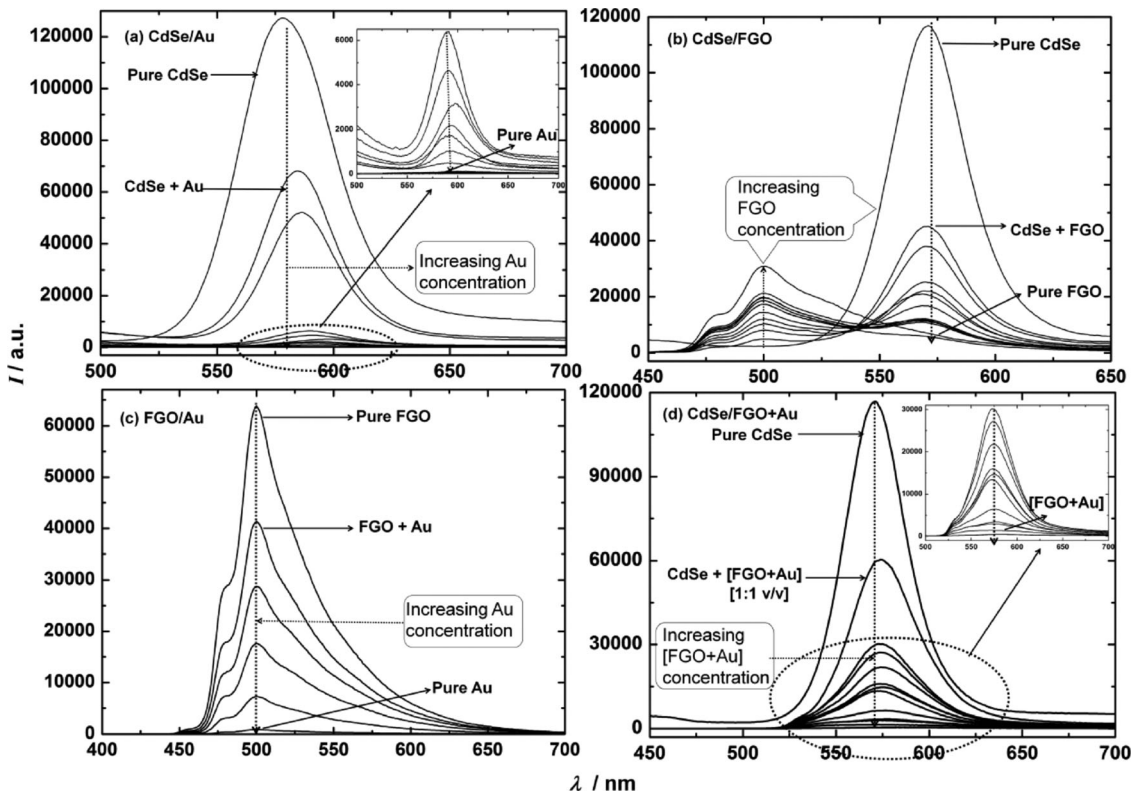

Fig. 3 Photoluminescence spectra of colloids: (a) CdSe QDs + Au NPs (b) CdSe QDs + FGO nanosheets, (c) FGO nanosheets + Au NPs and (d) CdSe QDs + [Au NPs + FGO nanosheets (1 : 1 v/v)] measured with λ_{ex} fixed at 370 nm. Initial colloid strengths: CdSe QDs: 3 mM, Au NPs: 4 mM and FGO nanosheets: 0.11 mg per mL; all in toluene. The total volume of pure colloids was fixed at 3000 μL, and aliquots of Au NPs or FGO nanosheets or [Au NPs + FGO nanosheets (1 : 1 v/v)] were added in steps of 50 μL, and progressive fluorescence decay of CdSe QDs was measured in (a, b and d) and of FGO nanosheets in (c).

CdSe QDs, observed at 570 nm, quenches dramatically, upon addition of FGO, for upon introduction of only 50 μL of FGO suspension to CdSe, CdSe emission intensity reduces to ~38% of its original value. This is an indicator of rapid charge transfer from CdSe QDs to the Fermi level of FGO. The quenching of the CdSe QD emission, as a function of increasing FGO content, is accompanied by the appearance and preponderance of a rather asymmetric emission peak of FGO centered at ~500 nm; the latter situation arises at high FGO content. Since the intensity of neat FGO emission is relatively much lower, approximately four times lesser as compared to that of neat CdSe QDs, it is reasonable to assume that electron transfer occurs from the dot to FGO. This is also supported by a previous study,[26] wherein RGO has been shown to be an excellent electron conduit material, when used in conjunction with TiO_2 and Ag nanoparticles,[27] for it was deduced to be efficient at both charge collection and transport. Neat Au NPs do not show any emission in the visible range (inset of Fig. 3a), and therefore, we observed a quenching of the photoluminescence (PL) peak of neat FGO nanosheets' suspension (0.11 mg per mL of toluene), when a 4 mM Au NP dispersion was introduced to the same (Fig. 3c). The diminishing intensity of FGO's emission peak with increasing Au NP content again hints at electron propagation from FGO nanosheets to Au NPs. Metal nanoparticles are known to behave as electron sinks, and when brought in contact with a semiconductor like FGO nanosheets (for unlike graphene, GO or RGO are not necessarily zero gap materials[37]), the Au NPs act as electron acceptors. As our composite is made of TiO_2/CdSe/FGO/Au, and since neat CdSe QDs show a strong emission at 570 nm, we studied the effect of a dispersion of a fixed composition, comprising FGO nanosheets (0.11 mg in 1 mL of toluene) and 4 mM Au NPs mixed in a 1 : 1 v/v ratio, on the PL peak of CdSe QDs (Fig. 3d). As anticipated, the intensity of the PL peak of neat CdSe QDs drops, with increasing concentration of this dispersion. It is evident that the photogenerated charge is transferred from CdSe QDs to the dispersion. Unlike the CdSe QDs/FGO nanosheet suspensions, where the emission due to FGO nanosheets tends to predominate at high FGO levels, here, we observed only a weak emission ascribable to FGO at ~525 nm (inset of Fig. 3d), which gains intensity at the expense of the CdSe QD emission. However, this emission due to FGO nanosheets remains rather weak, even at a fairly high content of the binary dispersion (Au NPs + FGO nanosheets: CdSe QDs ≈ 2 : 1 v/v), owing to the fact that in the binary mixture, the non-emissive Au NPs override the contribution of FGO nanosheets.

2.3 Emission decay analyses

To unambiguously ascertain that the interaction between the constituents of the following three systems: (i) CdSe and FGO, (ii) CdSe and Au and (iii) CdSe, FGO and Au is truly responsible for the emission quenching of excited CdSe, then the phenomena should be time-resolvable by following emission decay. We measured the emission decay profiles of the following films: TiO_2/CdSe, TiO_2/CdSe/FGO, TiO_2/CdSe/Au and TiO_2/CdSe/FGO/Au films and the corresponding plots are shown in Fig. 4 and Fig. S5 (ESI†). We preferred using films, instead of

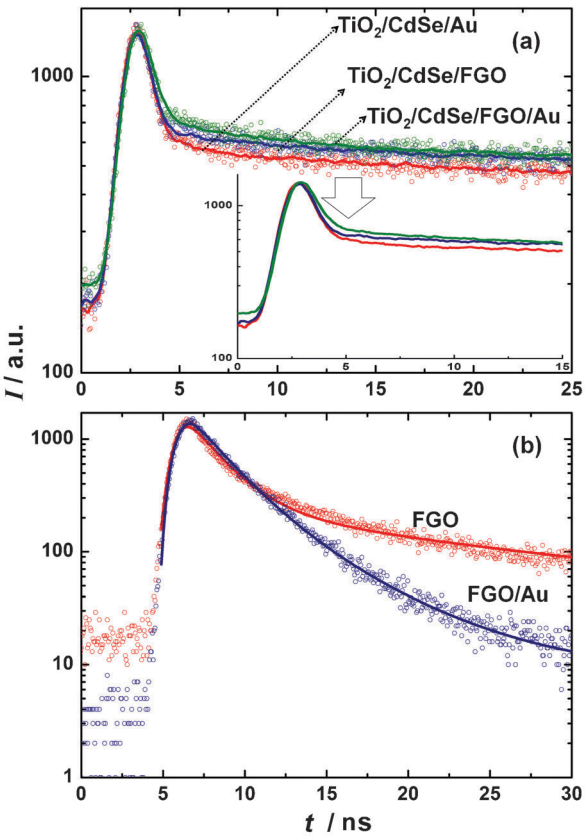

Fig. 4 Time resolved fluorescence decay profiles of (a) TiO_2/CdSe/Au, TiO_2/CdSe/FGO and TiO_2/CdSe/FGO/Au composite films and (b) a dispersion of FGO nanosheets and [FGO nanosheets + Au NPs] in toluene. Excitation for (a) and (b) were fixed at 370 nm and emission profiles were monitored for (a) and (b) at 570 and 500 nm respectively. The solid lines represent the best fits obtained by deconvolution, assuming bi-exponential decay.

dispersions, as films and not colloids are employed in photoelectrochemical cells and therefore, the extrapolation of the response obtained herein, to a practical functional cell based on the aforesaid films, would be justified. Since FGO when incorporated in the TiO_2 matrix, and utilized in the film form did not yield any reasonable fluorescence, probably due to a low content of active emissive sites, the measurements were confined to CdSe emission decay. The fluorescence thus obtained was fit to exponential curves to derive decay time constants, and this was also used to determine the average fluorescence times. The fluorescence decay is bi-exponential, in all cases, and it was analyzed using eqn (1) and the average lifetimes were estimated using eqn (2), where τ_i and B_i are time constants and amplitudes, respectively, of the individual decay components.

$$f(t) = B_1 e_1^{t/\tau} + B_2 e_2^{t/\tau} \quad (1)$$

$$\langle \tau \rangle = \Sigma_i B_i \tau_i / \Sigma_i B_i \quad (2)$$

Deconvolution was also attempted with three or four exponentials, as semiconductor nanocrystals are known to exhibit multi-exponential decay,[38] but it did not yield acceptable results, when judged from the χ^2 values and the plots of the residuals. The magnitudes of lifetimes (τ_1 and τ_2), the pre-exponential

Table 1 Fluorescence lifetimes of composite films (measured at λ_{ex} = 370 nm and λ_{em} = 570 nm) and solutions (measured at λ_{ex} = 370 nm and λ_{em} = 500 nm) deduced from double exponential fits[a]

Sample	χ^2	τ_1/ns	τ_2/ns	B_1	B_2	$\langle\tau\rangle$/ns
TiO_2/CdSe	1.225	1.616	12.72	30.23	69.77	9.363
TiO_2/CdSe/FGO	0.988	0.372	16.02	46.88	53.12	8.684
TiO_2/CdSe/Au	0.971	0.273	14.86	47.95	52.05	7.865
TiO_2/CdSe/FGO/Au	0.991	0.289	12.42	44.64	53.36	6.756
FGO	1.402	2.034	17.02	48.36	51.64	9.772
FGO/Au	1.256	2.225	5.375	63.94	36.96	4.859

[a] B is the relative amplitude of each lifetime, τ_1 and τ_2 are the fast and slow components of fluorescence lifetime and χ^2 represents the quality of fit.

terms (B_1 and B_2) and the average lifetimes ($\langle\tau\rangle$) are collated in Table 1. While the fast component of the fluorescence decay profile was found to decrease slightly on going from TiO_2/CdSe/FGO (0.372 ns) to TiO_2/CdSe/FGO/Au (0.289 ns) or TiO_2/CdSe/Au (0.273 ns), the slow component showed the reverse behavior. The longer lasting component had a lifetime of 16.02 ns for TiO_2/CdSe/FGO, 14.86 ns for TiO_2/CdSe/Au and it decreased to 12.42 ns for the TiO_2/CdSe/FGO/Au composite. Upon band gap excitation, charge separation in CdSe QDs is followed by electron–hole recombination, to yield emission. For the film of TiO_2/CdSe, without FGO or Au, the fast component in particular, compared to any of the composite with FGO nanosheets and/or Au NPs, was characterized by a much longer lifetime, greater by an order of magnitude, with a value of 1.616 ns, indicating that Au or FGO promote electron transfer (Fig. S5, ESI†). When CdSe QDs are molecularly linked to the TiO_2 surface, electron transfer from CdSe to TiO_2 occurs, and this process is driven by the differential in the conduction band edges of the two. However, an enhanced decay rate is achieved, when FGO nanosheets or Au NPs are an integral part of the film, as dictated by a more negative CB position of FGO or Au, with respect to the vacuum level. Here, we deduced an average lifetime of TiO_2/CdSe/Au emission to be 7.865 ns, and on replacing Au with FGO, the lifetime increased to 8.684 ns, for the composite TiO_2/CdSe/FGO, indicating that charge transfer from CdSe to Au *via* TiO_2 is faster than the transfer from CdSe to TiO_2 to FGO. Since the average lifetime for the TiO_2/CdSe/FGO/Au composite of 6.756 ns was the lowest, among all, it is a clear indicator of the fact that charge transfer is more efficient and rapid for the ternary combination of CdSe QDs, FGO nanosheets and Au NPs, tethered to TiO_2 rather than in the binary systems of CdSe QDs and Au NPs and CdSe QDs and FGO nanosheets flanked to the TiO_2 support.

Since we observed an enhanced decay rate in the TiO_2/CdSe/FGO/Au composite, the average emission lifetimes were therefore employed to estimate the rate of electron transfer, so as to include both the short- and long-lived components. The rate of electron transfer was obtained from the expressions:

$$k = 1/\langle\tau\rangle\ (TiO_2/CdSe/FGO/Au) - 1/\langle\tau\rangle\ (TiO_2/CdSe/FGO) \quad (3)$$

or

$$k = 1/\langle\tau\rangle\ (TiO_2/CdSe/FGO/Au) - 1/\langle\tau\rangle\ (TiO_2/CdSe/Au) \quad (4)$$

The apparent electron transfer rate (k) is deduced to be 3.3×10^7 s^{-1} and 2.1×10^7 s^{-1} from eqn (3) and (4), respectively, and since the two values are close, it is a reasonably good estimate. Our values also agree well with reported values for CdSe linked to TiO_2, typically varying between 10^7 to 10^{10} s^{-1}, depending on the QD size.[39] Furthermore, to affirm that electron transfer indeed occurs from FGO nanosheets to Au NPs, we compared the average emission lifetimes of neat FGO nanosheets with that of FGO nanosheets coupled with Au NPs, in solution phase. The average lifetime of neat FGO nanosheets' emission is 9.772 ns and it decreased to 4.859 ns, when Au NPs are added to FGO nanosheets. The reduction in lifetime by almost half of its original value confirms the fast charge transfer from FGO nanosheets to Au NPs. The rate constant for this electron transfer kinetics was determined from the following relation, in concurrence with a previous study on ZnO/GO composites:[38]

$$k = 1/\langle\tau\rangle\ (FGO/Au\ NPs) - 1/\langle\tau\rangle\ (FGO) \quad (5)$$

The rate constant of 10.35×10^7 s^{-1} in the FGO/Au NPs system is, in principle, higher than that observed for the TiO_2/CdSe/FGO/Au composite, but nevertheless, it validates the electron transfer mechanism proposed through Fig. 5. The energy band diagram, illustrating the electron transfer pathway in the composite, dictated by the relative positions of conduction band levels of the individual components, and the redox potential of the S^{2-}/S electrolyte, is shown in Fig. 5. The band gaps of CdSe QDs and TiO_2, and FGO nanosheets were determined from Tauc plots (Fig. S3, ESI†). The conduction band level of CdSe QDs with dimensions in the range of 3.5 to 4.0 nm lies at 3.9 eV, and it tends to be more negative with respect to the conduction band of TiO_2, on the NHE (Normal Hydrogen Electrode) scale.[40] Subsequent to illumination, the photogenerated electrons in CdSe QDs are transferred to the conduction band minimum of TiO_2 (4.2 eV). It can be seen that the offset of 0.22 eV between the conduction band minimum of TiO_2 and the work function of FGO (4.42 eV) is sufficient for charge separation, and since TiO_2 nanoparticles are in direct contact with FGO nanosheets, as was seen in the HRTEM images, the flow of excited electrons to FGO is facile.[26,41] Furthermore, graphene oxide sheets are known to function effectively as electron conduction supports, as they store as well as shuttle electrons.[27] Since, here, we obtained a fairly homogeneous distribution of TiO_2, Au NPs and CdSe QDs on the FGO nanosheets, the proposed electron transfer process is feasible. Au NPs, especially, when brought in contact with a semiconductor, upon Fermi level equilibration, tend to act as electron acceptors and can serve as electron sinks.[28] The work function of neat Au lies at ~5.1 eV,[42] but upon coming in contact with the TiO_2/CdSe/FGO, the apparent Fermi level (E'_F) is expected to be less negative with reference to vacuum, and as we achieved higher photocurrent in this quaternary system. Therefore upon Fermi level equilibration and illumination, as Au NPs tend to store electrons near the conduction band edge of the semiconductor,[43] E'_F should in principle lie between the work function of the conducting surface (SnO_2:F) and FGO, as shown in Fig. 5. The energetics of the TiO_2/CdSe/FGO/Au composite system

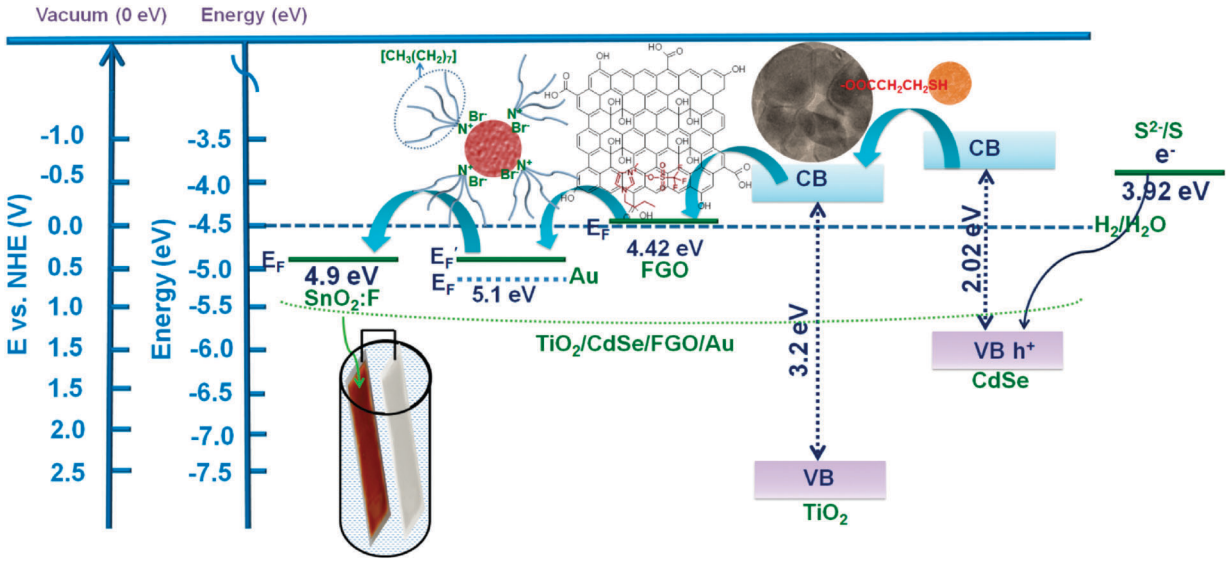

Fig. 5 Schematic showing the energy band diagram of the TiO_2/CdSe/FGO/Au composite and possible mode of electron transfer. Cartoon on the left hand side displays the cell with the digital photograph of the TiO_2/CdSe/FGO/Au composite film as the photoanode.

enables Au NPs to form a conduction bridge between FGO nanosheets and the current collector (FTO), thus allowing the passage of electrons to the external circuit. Since we found ample support, from microscopy results, for TiO_2/CdSe and Au NPs to be tethered to FGO nanosheets, FGO nanosheets therefore behave as scaffolds for the threesome, and this provides credence to the claim that electron transport to the external circuit has to occur through FGO nanosheets. Such a stepwise electron propagation process, therefore, accounts for the higher photocurrents and photovoltage achieved in this quaternary composite, in contrast to TiO_2/CdSe/FGO or TiO_2/CdSe/Au. Although the exact roles of FGO nanosheets and Au NPs are not very clear, but it is apparent that both work in synergy, and in particular their intrinsic ability to conduct electrons improves charge separation, for had it been otherwise, we would have achieved higher photocurrents/photovoltage and a faster decay rate in either TiO_2/CdSe/FGO or TiO_2/CdSe/Au composite.

2.4 Conducting atomic force microscopy (C-AFM) studies

C-AFM was employed for evaluating the nanoscale transport properties of the TiO_2/CdSe/FGO/Au composite, as it enables a correlation between the topographical features of the film with its ability to conduct electrons across the cross-section. Surface areas of the order of 100 μm^2 and 1 μm^2 were scanned (Fig. 6a′ and b′), and the nanoscale *I–V* characteristics were measured, at fifteen different points on the corresponding current images, in point contact mode. The corresponding current cross sections obtained along the lines in the current images are shown in Fig. 6a and b; since the profiles do show continuous spikes, fairly high currents are retained across the cross-section. The *I–V* curves shown in Fig. 6a″ and b″ are the resultant scans, obtained after averaging fifteen scans in each image. When the composite film is poised to a positive bias, excited electrons in the composite are attracted to the positive bias, such that there is a continuous supply of available levels in the composite, in the vicinity of the contact, for other electrons to occupy. These electrons diffuse towards the point contact and therefore the current is high. Under negative bias, electrons are injected into the available acceptor levels in the conduction band of the composite, they create a barrier, and hinder further electron flow. As a consequence, currents are low. At low field strengths, in the −5 V to +5 V regime (top inset of Fig. 6a″) and between +2.5 V to +7 V (inset of Fig. 6b″), the current density (*J*) and voltage are related by Ohm's law, as

$$J = q\mu nV/d \quad (6)$$

where *q* is the charge, μ is the electron mobility, *n* is the free charge carrier density, *V* is the applied bias and *d* is the sample thickness. The average nanoscale photoconductivity was deduced to be 0.031 S cm^{-1}, indicating the highly conducting nature of the film, and the presence of uniformly distributed conducting domains in the composite. It is obvious from both Fig. 6a″ and b″ that at low fields, when carriers are introduced, the Fermi level tends to shift towards the conduction band, carriers are trapped in the shallow traps and their contribution to current is minimal. At high fields, however, the Fermi level reaches the trap level, and current shows a sharp increase, since all new carriers introduced can reach the conducting band and current rises which is consistent with the change in slope. The defect sites in CdSe QDS act as traps. At high fields, the concentration of injected carriers exceeds the concentration of carriers produced by band gap excitation, and so the injected carriers are free and therefore mobile, others are mainly intrinsic, trapped and rendered immobile. Interestingly, we found that the high field *I–V* data gave a good fit to Dawber's diffusion model for electron conduction.[44] The equation approximates to $\log(I/V) = \text{constant} \times V^2$, which implies a slope of 2 for a $\log(\log(I/V))$ *versus* $\log V$ plot. Experimentally, we achieved a slope of 1.95 in the high potential region for this plot (bottom inset of Fig. 6a″) indicating an agreement with Dawber's equation. Both photoconductivity and *I–V* characteristics show that electrons are accepted and transported *via* the TiO_2/CdSe/FGO/Au network, from the C-AFM probe tip to

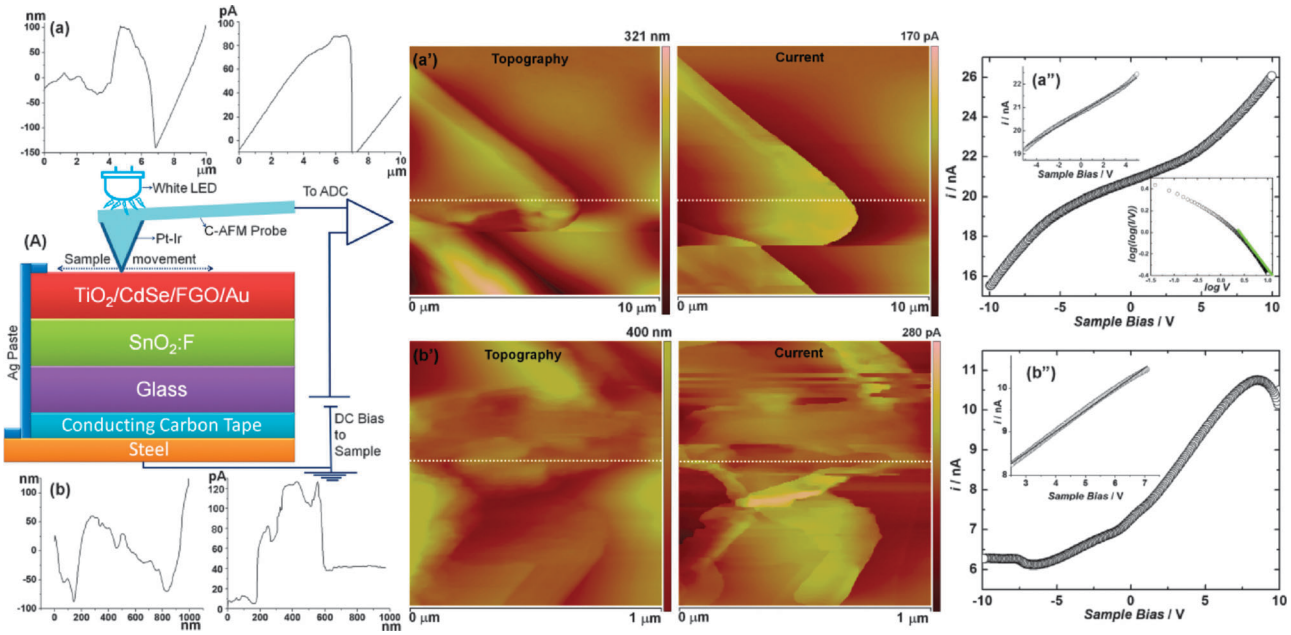

Fig. 6 (A) is a schematic of the configuration employed for C-AFM measurements. Representative current and topography images of the TiO_2/CdSe/FGO/Au composite film {a′ (scanned area: 100 μm^2) and b′ (scanned area: 1 μm^2)}, corresponding section images of topography and current, taken along the dotted lines are shown in a and b, a′′ and b′′ are point contact *I–V* curves averaged over fifteen scans from fifteen points on the current images shown in a′ and b′. Top inset of a′′ shows the linear fit between −5 to +5 V and bottom inset of a′′ shows the log(log(*I*/*V*)) *versus* log *V* response. Inset of b′′ shows the ohmic dependence between +2.5 and +7 V.

FTO, thereby reiterating that the organization of the nanomoieties in the composite is conducive for facile electron conduction.

2.5 Photoelectrochemistry of cells

Photovoltage generation (on–off cycles) for photoelectrochemical cells, based on composite films, as the photoanode, a platinum sheet as the counter electrode and an aqueous 0.1 M Na_2S solution as the electrolyte, is shown in Fig. 7A. The plots were recorded under a step time of 100 s, when no current was applied to the cells. Upon illumination, the composite film TiO_2/CdSe/FGO/Au based cell showed a five-fold enhancement in photovoltage in comparison to the cell based on the TiO_2/CdSe film. The maximum photovoltage registered for the composite based cell is ~700 mV in contrast to a value of 150 mV observed for the TiO_2/CdSe cell. The composites TiO_2/CdSe/Au and TiO_2/CdSe/FGO showed intermediate values of photovoltage, 590 mV and 400 mV, respectively. Photovoltage is higher in the TiO_2/CdSe/Au and TiO_2/CdSe/FGO composites, as compared to the TiO_2/CdSe cell. Since photovoltage is largely governed by the position of conduction band minimum or Fermi level, it is obvious that it moves to more negative potentials with respect to NHE, in the composites based on FGO nanosheets and/or Au NPs, in comparison to TiO_2/CdSe. The net Fermi level is known to move to more negative potentials, due to charge distribution between the two (in the present case: FGO/Au and TiO_2).[28] Such a high value of photovoltage has seldom been observed for similar nanocomposites. For a CdSe/TiO_2 system, a photovoltage >700 mV was obtained.[45] A photovoltage of 700 mV was obtained for a graphene/CdS QD cell, in contrast to a value close to 600 mV for a single walled carbon nanotube/CdS QD cell.[26] Authors[26] attributed the same to the capability of graphene nanosheets to allow a better distribution of QDs combined with a lower E_F difference between the sensitizer and the acceptor. The photocurrent on–off cycles recorded with respect to the zero external bias are shown in Fig. 7B. Here, the effect of FGO nanosheets and Au NPs is rather pronounced, as the TiO_2/CdSe/FGO/Au composite based cell acquires a maximum current of 400 μA, followed by TiO_2/CdSe/Au and TiO_2/CdSe/FGO composite based cells that show photocurrents of 70 and 10 μA respectively. For graphene/CdS QDs, a photocurrent of ~1.5 mA cm^{-2} was achieved[26] and for a CdSe/TiO_2 system, a photocurrent density of the same order was observed, however, for a less than unit square of illuminated electrode area.[32] Here, more than the absolute magnitude, the photocurrent produced by TiO_2/CdSe/FGO/Au is almost 6 times the value of TiO_2/CdSe/Au, again ratifying the effective role of FGO nanosheets in separating photogenerated electron–hole pairs and transferring the electrons to the electrode surface.

The dependence of photocurrent on applied potential for composite based photoelectrochemical cells is shown in Fig. 8a. Under open circuit voltage conditions, the Fermi level of Au NPs or FGO nanosheets is in equilibrium with the conducting band of SnO_2:F, in the presence of the redox electrolyte, by transferring excess charge to the S^{2-}/S couple, and electron flow is blocked. Thereafter, the photocurrent increases progressively with potential for all the three cells under illumination. *I–V* characteristics of the TiO_2/CdSe/FGO/Au composite based cell, shown in Fig. 8a, revealed a short circuit current (I_{SC}) of 200 μA and an open circuit voltage (V_{OC}) of 780 mV. A zero current potential of 640 mV

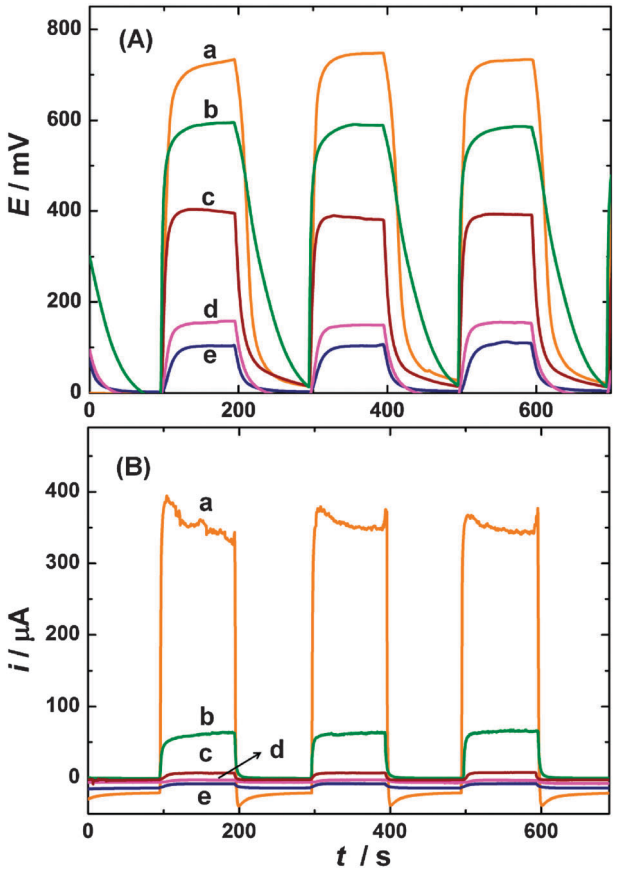

Fig. 7 (A) Photovoltage and (B) photocurrent on–off cycles for photoelectrochemical cells based on (a) TiO_2/CdSe/FGO/Au, (b) TiO_2/CdSe/Au, (c) TiO_2/CdSe/FGO, (d) TiO_2/CdSe, and (e) TiO_2 films as photoanodes. Counter electrode: Pt, electrolyte: aqueous 0.1 M Na_2S, under illumination at $\lambda > 300$ nm and input power of 100 mW cm^{-2}. Measurements were performed under zero applied current or bias.

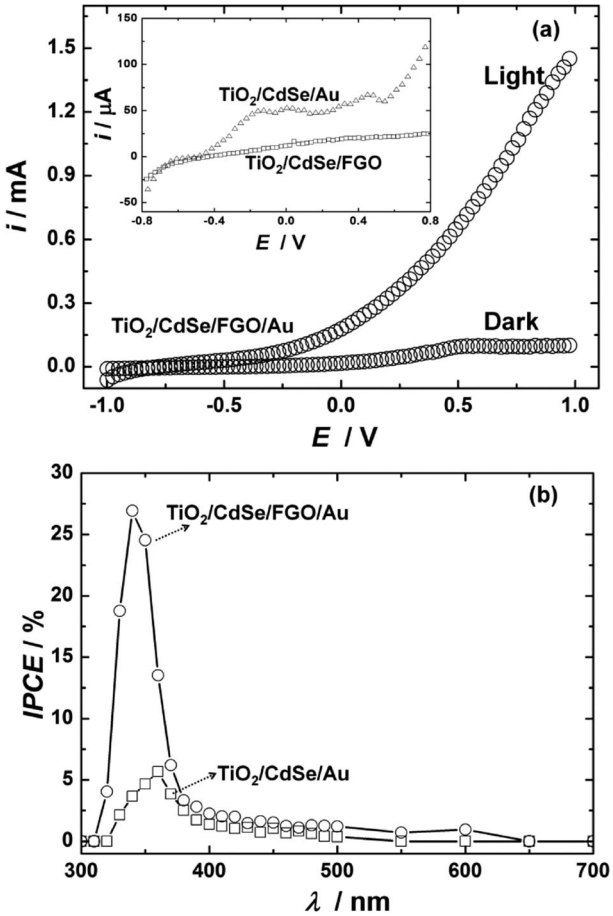

Fig. 8 (a) *I–V* characteristics of TiO_2/CdSe/FGO/Au composite based photoelectrochemical cells in light and dark; inset shows *I–V* plots of TiO_2/CdSe/Au (△) TiO_2/CdSe/FGO (□) recorded at $\lambda > 300$ nm, at 100 mW cm^{-2} irradiant power and (b) photoaction spectra of TiO_2/CdSe/FGO/Au (○) and TiO_2/CdSe/Au (□) based cells. In a and b: counter electrode: Pt, electrolyte: aqueous 0.1 M Na_2S.

was registered for the CdSe/TiO_2 cell, based on a Co(II/III) redox couple as an electrolyte.[15] An open circuit voltage of 650 ± 20 mV was observed for all CdSe/TiO_2 based electrodes upon excitation with visible light ($\lambda > 420$ nm).[43] Although higher short circuit current densities were achieved in the CdSe/TiO_2–Co(II/III) system, the photocurrent maximum acquired by the TiO_2/CdSe/FGO/Au composite based cell ($I = 1.16$ mA at $E = +0.8$ V) shows a nearly 9-fold enhancement as compared to the neat TiO_2/CdSe/Au cell ($I = 0.125$ mA at $E = +0.8$ V). I_{SC} is much smaller for TiO_2/CdSe/Au (56 μA) and TiO_2/CdSe/FGO (14 μA) composite based cells, indicating that the stepwise electron transfer process from the conduction band of TiO_2 to FGO to Au is exergonic while that from TiO_2 to FGO or TiO_2 to Au alone is endergonic.[24] In the composite TiO_2/CdSe/FGO/Au, increased charge separation is due to a significantly lowered rate of charge recombination, as (i) photogenerated electrons are rapidly scavenged by FGO, which has the capacity to store electrons and (ii) also by the ability of Au nanoparticles to quickly convey them to the current collector.

The photoaction spectra of the two cells, capable of producing highest photocurrents, are compared in Fig. 8b. The photocurrents were much higher for the TiO_2/CdSe/FGO/Au composite based cell in the photopic region as compared to that shown by the TiO_2/CdSe/Au cell, indicating the cumulative effect of FGO nanosheets and Au NPs in improving the current response. The incident photon to current conversion efficiency (IPCE) of TiO_2/CdSe/FGO/Au is 4.5 times more than that of TiO_2/CdSe/Au, indicating that graphene nanostructures facilitate charge movement. For a system of Au/TiO_2 sensitized with CdSe QDs, a maximum IPCE slightly less than 25% was registered as opposed to a value of about 6% obtained for the CdSe/TiO_2 system,[29] and the value was less than 2.5% in the visible region for both films. For a CdTe/TiO_2 system, the IPCE was about 3% at ~400 nm.[32] For a CdSe(ZnS)–Au/TiO_2 system, an IPCE greater than 20% was achieved at $\lambda <$ 400 nm.[46] However, an IPCE in the range of 15–20% was retained up to 550 nm. For a system of CdS QDs sensitized onto graphene an IPCE of ~16% was obtained at 350 nm,[26] authors demonstrated the superiority of graphene nanostructures for generating higher photocurrents in QD based photoanodes, as compared to single walled carbon nanotubes. It is evident that the combination of FGO nanosheets and Au NPs provides a less resistive conduction pathway, through the coating and thus enhances the photoelectro chemical activity.

3. Experimental

3.1 Chemicals

Selenium powder (Se), trioctyl phosphine oxide ($OP(C_8H_{17})_3$, TOPO), trioctyl phosphine ($P(C_8H_{17})_3$, TOP), hydrogen tetrachloroaurate ($HAuCl_4$), titanium oxide (TiO_2, <25 nm) were purchased from Aldrich. Cadmium acetate dehydrate ($Cd(CH_3COO)_2{\cdot}2H_2O$), sodium borohydride ($NaBH_4$), sodium sulfate ($Na_2SO_4$), sodium sulfide ($Na_2S$), mercaptopropionic acid (MPA), tetraoctylammonium bromide, and 1-butyl-3-methyl-imidazolium trifluoromethanesulfonate were procured from Merck. Solvents: deionized water (resistivity $\approx$ 18.2 MΩ cm) was obtained through a Millipore Direct-Q 3 UV system, toluene, dimethyl formamide (DMF) absolute ethanol were obtained from Merck and used as received. Inorganic transparent electrodes of SnO_2 : F coated glass (FTO, Pilkington, sheet resistance: 14 Ω per sq) were cleaned in a soap solution, 30% HCl solution, double distilled water and acetone prior to use.

3.2 Synthesis of CdSe QDs

CdSe nanocrystal QDs were prepared by using a chemical route procedure reported previously involving the TOPO/TOP capping method.[47] Briefly, selenium (Se) solution was prepared by mixing 0.40 g of Se powder, 10 mL of TOP, and 0.20 mL of toluene. 20 g of technical-grade TOPO and 0.25 g of cadmium acetate dihydrate were taken in a three-neck, round-bottomed flask and stirred for 10 minutes at about 150 °C. After the solution was degassed and purged with nitrogen at this temperature, it was then heated to 300 °C. At this temperature, the selenium solution was immediately injected to the flask. The solution was heated at 300 °C for only 2 minutes to arrest the quantum dot size, which was accompanied by a color change from yellow to red. The resulting red colored solution was cooled to room temperature and an excess amount of ethanol was added to the solution, to precipitate the quantum dots. In order to remove the superfluous TOPO, the precipitated QDs were re-dissolved in a small quantity of toluene and re-precipitated in ethanol. The procedure was repeated for two more times and the liquid portion (ethanol) was discarded upon centrifugation, and the precipitate was stored under nitrogen.

3.3 Synthesis of gold nanoparticle dispersion

A suspension of Au NPs in toluene was prepared by the method developed by Brust *et al.*[48] Two solutions, one containing $HAuCl_4$ (0.18 g) in 15 mL of deionized water and another composed of tetraoctylammoniumbromide (1.09 g) in 40 mL of toluene, were prepared. The two solutions were mixed and stirred continuously for about 10 minutes until the color of the aqueous phase became clear and thereafter, a solution of $NaBH_4$ (0.4 M) in deionized water was added slowly and carefully to the toluene phase with continuous stirring. The color of the upper organic phase changed from orange to ruby red whereas the lower aqueous phase turned colorless. The mixture was stirred for 30 more minutes. The organic phase containing Au NPs was extracted, washed once with dilute sulfuric acid for neutralization and subsequently five times with distilled water, and then dried over anhydrous sodium sulfate. The strength of the resulting ruby red dispersion was 4 mM, assuming the complete reduction of $HAuCl_4$ to Au. It was stored in dark at room temperature.

3.4 Synthesis of functionalized graphene oxide from graphite rods

1-Butyl-3-methyl-imidazolium trifluoromethanesulfonate and water were mixed in a 1 : 1 weight ratio and taken in a rectangular glass cell. Graphite rods were employed as both cathode and anode, and a fixed dc potential of 15 V was applied across the cell for 2 hours at room temperature. Exfoliation of the graphite rod occurs specifically at the anode. The expanded graphite rod was immersed in DMF intermittently. Graphene oxide, functionalized by the ionic liquid,[36] is transferred to the solvent, each time. It was collected by centrifugation, washed with DMF and ethanol, and dried at 50 °C, in an oven for 12 hours.

3.5 Fabrication of the QD sensitized electrodes

A thick slurry of TiO_2 anatase nano-powder and FGO (0.11 mg per mL of solvent) was prepared in ethanol. The resulting slurry was coated on FTO coated glass using a doctor blade method and annealed at 150 °C for 40 minutes to enable evaporation of the solvent and adherence of TiO_2/FGO to the substrate. The QD sensitized film was prepared by first keeping the TiO_2/FGO film immersed in a 0.1 M MPA linker solution in deionized water for 10–12 h. The substrate coated with TiO_2/linker was rinsed with ethanol repeatedly, to remove excess MPA. A dispersion of Au NPs (4 mM) and a solution of TOP/TOPO capped CdSe QDs (200 mM) were mixed in a 1 : 1 volume ratio and the TiO_2/linker coating was submerged in the resulting suspension for 10–12 h for anchoring of fine CdSe QDs and Au NPs vis-à-vis sulfur on the linker molecules. The resulting TiO_2/CdSe/FGO/Au electrode was washed with toluene and stored in the dark. The same protocols were employed for fabricating TiO_2/CdSe, TiO_2/CdSe/FGO and TiO_2/CdSe/Au electrodes.

3.6 Characterization techniques

TEM images were obtained on a HRTEM FEI Tecnai G^2 F30 STWIN with a FEG source at 300 kV. For TEM, a thin layer of the sample was carefully extracted using forceps in isopropanol and then transferred onto a carbon coated copper grid of 3.05 mm diameter and the solvent was evaporated. The optical absorption spectra of the CdSe QD solution and Au dispersion were measured in the visible region with respect to toluene in the reference beam, on a UV-Vis-NIR spectrophotometer (Shimadzu UV-3600). Diffuse reflectance spectra of TiO_2 were measured with the same instrument, using an integrating sphere with $BaSO_4$ in the reference beam; reflectance was converted to absorbance with Kubulka munk program. Photoluminescence spectra of the samples (films in a solid sample holder, inclined at 45°, with respect to the incident beam for maximizing the output intensity and solutions in quartz cuvettes) were recorded on a Horiba Fluoromax-4 fluorescence spectrometer; an appropriate filter was employed during the measurement and background correction was also applied. The Time-Correlated Single Photon Counting (TCSPC) method was used for determination of emission lifetimes using the

Horiba Jobin Yvon Data Station HUB operating in the TCSPC mode. A nanoLED diode emitting pulses at 370 nm with 1 MHz repetition rate and a pulse duration of 1.3 ns was used as an excitation source. Light-scattering Ludox solution (colloidal silica) was utilized to obtain the instrument response function (prompt). For all the measured samples, a long pass 500 nm filter was placed in front of the emission monochromator. Horiba Jobin Yvon DAS6 fluorescence decay analysis software was used to fit the model function (two-exponential decays) to the experimental data, with appropriate correction for the instrument response. A 1000 W tungsten–halogen lamp (Osram) was employed as an excitation source and the intensity incident on the measuring cell was adjusted with respect to a reference standard Si solar cell to approximately one sun (100 mW cm^{-2}). Photocurrent/photovoltage *versus* time plots and illuminated *I–V* characteristics were measured for photoelectrochemical cells, comprising composite films deposited on SnO_2 : F coated glass as photoanodes, a Pt sheet as a counter electrode in a 0.1 M Na_2S aqueous electrolyte, on an Autolab Potentiostat/Galvanostat coupled with Nova 1.6 software. For cells in a similar configuration, consisting of an active photoanode area of 1 cm^2, incident photon to current conversion efficiencies (IPCE) were obtained on an electrochemical workstation PARSTAT 2273. A 450 W Oriel Xenon arc lamp was employed as the light source, coupled with a monochromator Newport 74125 placed in the light path, and at different excitation wavelengths in the 300–700 nm range, chronoamperometry curves were recorded. IPCE values were determined using eqn (7), where J_{SC} is the short circuit current density and I is the incident power.

$$\text{IPCE (\%)} = J_{SC}\ (\text{A cm}^{-2}) \times 124000/\lambda\ (\text{nm}) \times I\ (\text{W cm}^{-2}) \quad (7)$$

A Conductive Atomic Force Microscope (AFM, Veeco Multimode 8) equipped with a current sensing module was used to generate current and topography images simultaneously. Platinum–Iridium (20 nm) coated cantilevers made of antimony doped silicon (n-doped; resistivity $\approx$ 0.01–0.025 Ω cm) were purchased from Veeco. A bias voltage of $\sim$2 V was applied between the conducting tip (which was grounded) and the sample during imaging. The load force was maintained at 49 nN during the measurement to avoid any damage to the sample or the tip. The current sensitivity was 1 nA V^{-1}. TiO_2/CdSe/FGO/Au composite deposited on SnO_2 : F coated glass was flanked to a stainless steel disc with a thin conducting carbon tape. A continuous strip of silver paste was applied evenly and carefully, running from the surface of the sample, along the edge of the conducting substrate to the stainless steel mount, to enable the measurement, which was performed under ambient conditions. Due care was taken to ensure that no cracks were formed on the silver paste coating, upon drying, in order to maintain a continuous contact, during the measurement. Point contact *I–V* characteristics were measured between + 10 V and –10 V. A white LED adjusted to deliver a light intensity of 100 mW cm^{-2} on the sample surface was employed as the light source.

Conclusions

Photoelectrochemical cells based on TiO_2/CdSe/FGO/Au composites showed dramatically enhanced photovoltage and photocurrents as compared to TiO_2/CdSe/FGO and TiO_2/CdSe/Au composites. The successful anchoring of CdSe QDs, Au NPs and TiO_2 onto FGO nanosheets was confirmed from HRTEM. Progressive quenching of CdSe emission by Au NPs or FGO nanosheets and the time resolved fluorescence decay experiments provided evidences for rapid and facile electron transfer, in a step-wise manner, from CdSe QDs to TiO_2 to FGO to Au NPs in the composite, as a higher rate constant was achieved in TiO_2/CdSe/FGO/Au, in comparison to TiO_2/CdSe/FGO and TiO_2/CdSe/Au. Conductive-AFM also showed the presence of well-connected conducting domains in the composite, and a high average photoconductivity of 0.031 S cm^{-1} on the nanoscale, thus indicating the homogeneity of the deposit. Combining FGO nanosheets with Au NPs yields an assembly most conducive for a fast electron injection rate; it enables the formation of photoelectrochemical cells capable of producing a photovoltage greater than 100 mV, and photocurrent nearly 6 times higher than that of a TiO_2/CdSe/Au based cell. An IPCE of 27% achieved for the composite confirms that the integration of electron conduit materials like FGO nanosheets and Au NPs allows efficient electron transport, probably by the virtue of high quality interfaces generated between the four components. Further studies are necessary to directly correlate the interfacial properties, and composition with electron injection dynamics and photoelectrochemical response. This method provides a convenient way to achieve a fairly uniform distribution of the electron conducting (FGO nanosheets and Au NPs) and the photoactive (CdSe QDs linked to TiO_2) materials for only such interpenetrating networks can account for the high photocurrent registered herein. Such an architecture of donor–acceptor assembly, as fabricated here, also offers the benefit of an offset between the levels of different moieties, optimal for rapid electron injection and minimal electron–hole recombination. More studies are underway to acquire a deeper understanding of kinetics of electron transfer in systems based on photosensitive QDs coupled with electron acceptor materials.

Acknowledgements

Financial support from Department of Science and Technology (SR/S1/PC-06/2010) is gratefully acknowledged. We also thank Dr P.H. Borse, International Advanced Research Centre for Powder Metallurgy and New Materials (ARCI) for IPCE measurements.

References

1 S. Ruhle, M. Shalom and A. Zaban, *ChemPhysChem*, 2010, **11**, 2290–2304.
2 Y.-L. Lee, B.-M. Huang and H.-T. Chien, *Chem. Mater.*, 2008, **20**, 6903–6905.
3 N. Zhu, F. Su, T. Lv, L. Pan and Z. Sun, *Nanoscale Res. Lett.*, 2010, **5**, 1749–1754.
4 J. Chen, W. Lei and W. Q. Deng, *Nanoscale*, 2011, **3**, 674–677.
5 B. Ma, L. Wang, H. Dong, R. Gao, Y. Geng and Y. Z. Y. Qiu, *Phys. Chem. Chem. Phys.*, 2011, **13**, 2656–2658.
6 A. Zaban, O. I. Micic, B. A. Gregg and A. J. Nozik, *Langmuir*, 1998, **14**, 3153–3156.
7 L.-C. Chen, C.-C. Wang and B.-S. Tseng, *J. Optoelectron. Biomed. Mater.*, 2009, **1**, 249–254.

8 C.-Y. Kuo, M.-S. Su, C.-S. Ku, S.-M. Wang, H.-Y. Lee and K.-H. Wei, *J. Mater. Chem.*, 2011, **21**, 11605–11612.
9 D. Hu, C. C. McPheeters, E. T. Yu and D. M. Schaadt, *Nanoscale Res. Lett.*, 2011, **6**, 83–87.
10 I. Mora-Sero, S. Gimenez, F. Fabregat-Santiago, R. Gomez, Q. Shen, T. Toyoda and J. Bisquert, *Acc. Chem. Res.*, 2009, **42**, 1848–1857.
11 A. V. Firth, Y. Tao, D. Wang, J. Ding and F. Bensebaa, *J. Mater. Chem.*, 2005, **15**, 4367–4372.
12 P. Yu, K. Zhu, A. G. Norman, S. Ferrere, A. J. Frank and A. J. Nozik, *J. Phys. Chem. B*, 2006, **110**, 25451–25454.
13 Y. Tian and T. Tatsuma, *J. Am. Chem. Soc.*, 2005, **127**, 7632–7637.
14 S. Cazzanti, S. Caramori, R. Argazzi, C. M. Elliott and C. A. Bignozzi, *J. Am. Chem. Soc.*, 2006, **128**, 9996–9997.
15 H. J. Lee, J.-H. Yum, H. C. Leventis, S. M. Zakeeruddin, S. A. Haque, P. Chen, S. I. Seok, M. Gratzel and Md. K. Nazeeruddin, *J. Phys. Chem. C*, 2008, **112**, 11600–11608.
16 H. J. Lee, D. W. Chang, S. M. Park, S. M. Zakeeruddin, M. Gratzel and Md. K. Nazeeruddin, *Chem. Commun.*, 2010, **46**, 8788–8790.
17 S. Buhbut, S. Itzhakov, E. Tauber, M. Shalom, I. Hod, T. Geiger, Y. Garini, D. Oron and A. Zaban, *ACS Nano*, 2010, **4**, 1293–1298.
18 J. Chen, C. Li, G. Eda, Y. Zhang, W. Lei, M. Chhowalla, W. I. Milne and W. Q. Deng, *Chem. Commun.*, 2011, **47**, 6084–6086.
19 H. Hayashi, I. V. Lightcap, M. Tsujimoto, M. Takano, T. Umeyama, P. V. Kamat and H. Imahori, *J. Am. Chem. Soc.*, 2011, **133**, 7684–7687.
20 A. Salant, M. Shalom, I. Hod, A. Faust, A. Zaban and U. Banin, *ACS Nano*, 2010, **4**, 5962–5968.
21 N. Fuke, L. B. Hoch, A. Y. Koposov, V. W. Manner, D. J. Werder, A. Fukui, N. Koide, H. Katayama and M. Sykora, *ACS Nano*, 2010, **4**, 6377–6386.
22 B. X. Li, H. Zhu, K. Wang, A. Cao, J. Wei, C. Li, Y. Jia, Z. Li, X. Li and D. Wu, *Adv. Mater.*, 2010, **22**, 2743–2748.
23 Y. Sun, Q. Wu and G. Shi, *Energy Environ. Sci.*, 2011, **4**, 1113–1132.
24 T. Hasobe, S. Fukuzumi and P. V. Kamat, *Angew. Chem., Int. Ed.*, 2006, **45**, 755–759.
25 A. Kongkanand and P. V. Kamat, *ACS Nano*, 2007, **1**, 13–21.
26 C. X. Guo, H. B. Yang, Z. M. Sheng, Z. S. Lu, Q. L. Song and C. M. Li, *Angew. Chem., Int. Ed.*, 2010, **49**, 3014–3017.
27 I. V. Lightcap, T. H. Kosel and P. V. Kamat, *Nano Lett.*, 2010, **10**, 577–583.
28 M. Jakob, H. Levanon and P. V. Kamat, *Nano Lett.*, 2003, **3**, 353–358.
29 L. Liu, G. Wang, Y. Li, Y. Li and J. Z. Zhang, *Nano Res.*, 2010, **4**, 249–258.
30 S. Bhandari, M. Deepa, S. N. Sharma, A. G. Joshi, A. K. Srivastava and R. Kant, *J. Phys. Chem. C*, 2010, **114**, 14606–14613.
31 A. P. Saxena, M. Deepa, A. G. Joshi, S. Bhandari and A. K. Srivastava, *ACS Appl. Mater. Interfaces*, 2011, **3**, 1115–1126.
32 P. V. Kamat, *J. Phys. Chem. C*, 2008, **112**, 18737–18753.
33 J. H. Bang and P. V. Kamat, *ACS Nano*, 2009, **3**, 1467–1476.
34 P. K. Khanna, P. More, B. G. Bharate and A. K. Vishwanath, *J. Lumin.*, 2010, **130**, 18–23.
35 B. Farrow and P. V. Kamat, *J. Am. Chem. Soc.*, 2009, **131**, 11124–11131.
36 J. Lu, J.-X. Yang, J. Wang, A. Lim, S. Wang and K. P. Loh, *ACS Nano*, 2009, **3**, 2367–2375.
37 Y. Lin, K. Zhang, W. Chen, Y. Liu, Z. Geng, J. Zeng, N. Pan, L. Yan, X. Wang and J. G. Hou, *ACS Nano*, 2010, **4**, 3033–3038.
38 G. Williams and P. V. Kamat, *Langmuir*, 2009, **25**, 13869–13873.
39 I. Robel, M. Kuno and P. V. Kamat, *J. Am. Chem. Soc.*, 2007, **129**, 4136–4137.
40 H.-Y. Si, C.-H. Liu, H. Xu, T.-M. Wang and H.-L. Zhang, *Nanoscale Res. Lett.*, 2009, **4**, 1146–1152.
41 Y.-B. Tang, C.-S. Lee, J. Xu, Z.-T. Liu, Z.-H. Chen, Z. He, Y.-L. Cao, G. Yuan, H. Song, L. Chen, L. Luo, H.-M. Cheng, W.-J. Zhang, I. Bello and S.-T. Lee, *ACS Nano*, 2010, **4**, 3482–3488.
42 R. Costi, G. Cohen, A. Salant, E. Rabani and U. Banin, *Nano Lett.*, 2009, **9**, 2031–2039.
43 P. V. Kamat, *J. Phys. Chem. C*, 2008, **112**, 18737–18753.
44 F. D. Morrison, P. Zubko, D. J. Jung, J. F. Scott, P. Baxter, M. M. Saad, R. M. Bowman and J. M. Gregg, *Appl. Phys. Lett.*, 2005, **86**, 152903–152906.
45 A. Kongkanand, K. Tvrdy, K. Takechi, M. Kuno and P. V. Kamat, *J. Am. Chem. Soc.*, 2008, **130**, 4007–4015.
46 M.-H. Jung and M. G. Kang, *J. Mater. Chem.*, 2011, **21**, 2694–2700.
47 Z. A. Peng and X. Peng, *J. Am. Chem. Soc.*, 2002, **124**, 3343–3353.
48 M. Brust, M. Walker, D. Bethell, D. J. Schiffrin and R. Whyman, *J. Chem. Soc., Chem. Commun.*, 1994, 801–802.

